DIGITAL CORE LABORATORY: ROCK AND FLOW PROPERTIES DERIVED FROM COMPUTER GENERATED ROCKS

P.E. Øren, S. Bakke, and H.G. Rueslåtten
Numerical Rocks AS

This paper was prepared for presentation at the International Symposium of the Society of Core Analysts held in Trondheim, Norway 12-16 September, 2006

ABSTRACT

We use a geologically based reconstruction technique to generate virtual rocks of complex sandstone lithofacies in a North Sea oil reservoir. Effective properties of the computer generated rocks, such as fluid permeability, electrical resistivity, and elastic moduli, are compared with those determined from microtomographic images of the actual rocks. The comparison largely shows an excellent agreement. Using network modeling techniques, we compute waterflood relative permeabilities for the computer generated rocks and compare them with experimental data. The experimental core samples exhibited large differences in wettability with measured Amott indices ranging from 0.3 to 0.7. The physical origin for this variation is not known. However, our results demonstrate clearly that for a fixed pore level distribution of wettability, both the residual oil saturation and the Amott index increases with increasing initial water saturation. This is caused primarily by reduced oil film stability in mixed wet pores. The present study demonstrates the potential and feasibility of combining computer generated rocks with numerical calculations to derive important rock and flow properties for reservoir rocks.

INTRODUCTION

Due to great advancements in computer technology, macroscopic rock and transport properties can now be derived directly from three-dimensional (3D) images of the rock microstructure. Effective properties that can be numerically calculated include elastic moduli (Arns et al., 2002), electrical resistivities (Øren and Bakke, 2002), permeability (Jin et al., 2004, Arns *et al*., 2004), NMR relaxation (Øren *et al*., 2002, Knackstedt *et al*., 2004), mechanical properties (Jin *et al*., 2003), and constitutive relationships for two- and three-phase flow (Øren *et al*., 1998, Lerdahl, *et al*., 2000, Valvatne and Blunt, 2004, Piri and Blunt, 2005). The acquisition of detailed 3D representations of the pore structure of reservoir rocks is therefore of great practical importance to the petroleum industry.

In the past decades, several approaches have been proposed to acquire 3D representations of the microstructure of reservoir rocks. One commonly used method is stochastic reconstruction (Adler *et al*., 1990, Hazlett, 1997, Yeoung and Torquato, 1998). This technique relies on matching statistical properties of a 3D model to those measured on 2D thin section images of the actual rock. Recent quantitative comparisons of stochastic

reconstructions with microtomographic images have shown that stochastic models tend to underestimate the connectivity of the pore space and thus the permeability, particularly for low porosity samples (Biswal *et al*., 1999, Manswart *et al*., 2002, Øren and Bakke, 2003).

In recent years, process or geologically based reconstruction techniques have been established for the attainment of digitized representations of reservoir rock microstructures (Bryant *et al*., 1993, Bakke and Øren, 1997, Øren and Bakke, 2002, Jin *et al*., 2003). In short, these techniques are based on an explicit simulation of the geological rock-forming processes, i.e., sedimentation, compaction, and diagenetic overprinting. Necessary input parameters for the reconstruction are extracted from backscattered electron (BSE) images of 2D thin sections (Øren and Bakke, 2002).

In the present work, we use a geologically based reconstruction technique to generate virtual rocks of a complex sandstone lithofacies in a North Sea oil reservoir. We compute material and transport related effective properties of the computer generated rocks and compare them with those derived from X-ray microtomographic (micro-CT) images of the actual rock samples. Network modeling techniques are utilized to compute waterflood relative permeabilities for the reconstructed rocks. The predicted relative permeabilities are compared with experimental data.

SAMPLE CHARACTERIZATION

The presented reservoir rock samples are poorly consolidated sandstones with an average grain size diameter between 140 μm < d < 900 μm, a porosity ϕ of 0.23 to 0.27, and a permeability range between 1 and 10 Darcy. The depositional environment constitutes that of a fluvial channel setting. Hence the samples are heterogeneous and have in addition undergone complex diagenetic alteration, i.e., the formation of authigenic clay minerals (5-8%) and patchy carbonate cementation (see Figure 1). Special Core Analysis information for the rock type is available, including Amott wettability measurements, centrifuge measured oil relative permeabilities on three core plugs, and steady state relative permeabilities on two composite cores. The measured Amott wettability index, I_{wo}, for the rock type ranged from 0.3 to 0.7, with an average value of 0.5.

The porosity obtained from the BSE image in Figure 1 is 0.236. A mosaic of 256 such images from a thin section was employed to extract the necessary input parameters for the geologically based reconstruction of the sample. A total of 10 realizations of the rock type were generated by introducing small variations in the clay content and in the target porosity. A detailed description of the reconstruction algorithm and the applied procedures are given elsewhere (Bakke and Øren, 1997, Øren and Bakke, 2002, Øren and Bakke, 2003). High resolution micro-CT images were acquired from one representative sample of the rock type. The resolution of the micro-CT data is 5.24 μm for an extracted sample size of 10 mm in diameter. The microtomographic images were obtained from the Australian National University (Arns *et al*., 2004, Knackstedt *et al*., 2004).

Cross-sections of the microtomographic image, denoted MCT, and a reconstructed sample, denoted PBM, are compared in Figure 2. Both samples are voxel based with a size of 512^3 and a resolution of 5.24 μm. In the following, we compute and compare effective material and transport properties of these samples. Core plug measurements are given where they are available.

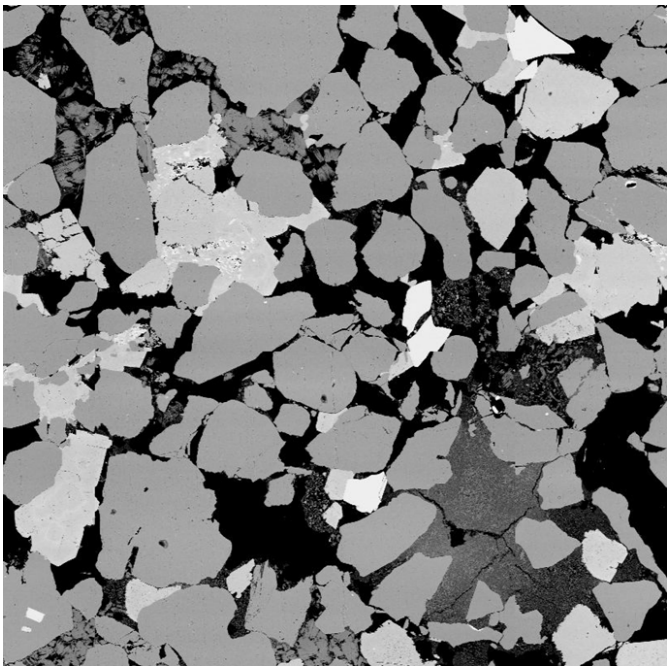

Figure 1. BSE image of a thin section from a heterogeneous North Sea reservoir sandstone, indicating pore space (black), clay (dark gray), quartz (gray), feldspar (lighter gray) and carbonate cement (light gray). The pixel resolution is 3.31 μm.

TRANSPORT PROPERTIES

Averaging of the local continuum equations relates the effects of the microstructure to the effective physical transport properties applicable at the macroscopic scale. For transport properties in homogenous media, a generalized flux associated with a conservable quantity (e.g., electrical current, stress, or momentum) is linearly related to a generalized gradient (electrical field, strain, pressure) with the proportionality constant K_e. For elasticity and electrical conduction, this may be written as $F(\mathbf{x}) = K_e(\mathbf{x}) \bullet G(\mathbf{x})$, where F obeys the differential equation $\nabla \cdot F(\mathbf{x}) = 0$. In heterogeneous media, we expect similar linear relations involving the averaged fields

$$\begin{aligned} \left[F(\mathbf{x})\right] &= K_e \cdot \left[G(\mathbf{x})\right] \quad \text{and} \\ \left[\mathbf{v}(\mathbf{x})\right] &= K_e \cdot g(\mathbf{x}) \qquad \text{with } K_e = -k/\mu \end{aligned} \tag{1}$$

for elasticity/conductivity and fluid permeability, respectively. Angular brackets denote an average operation such that K_e becomes an effective property, **v** denotes fluid velocity, g is an applied pressure gradient, k is absolute permeability, and μ is fluid viscosity.

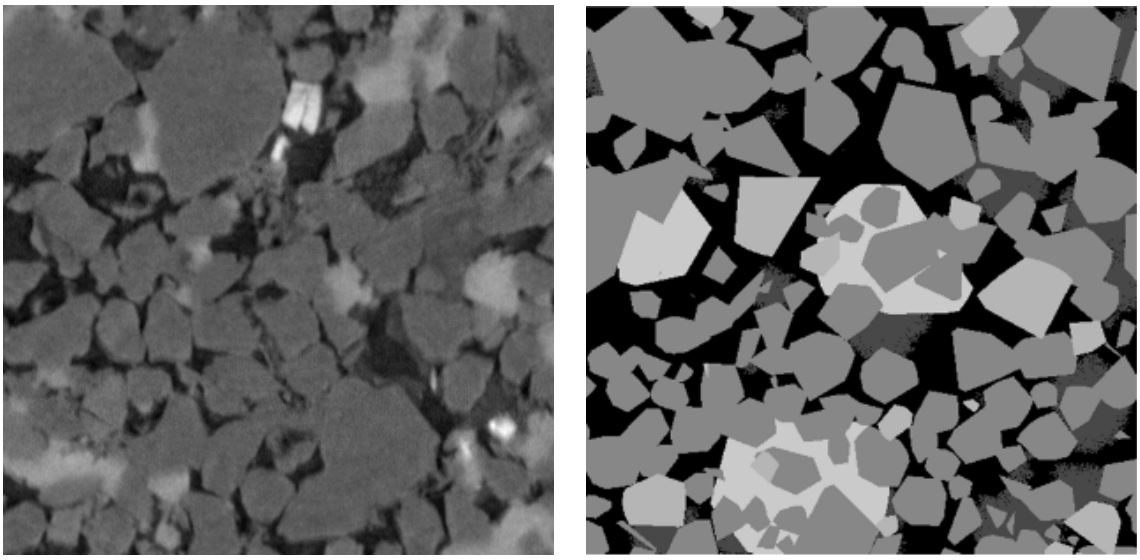

Figure 2. MCT image (left) and PBM reconstruction (right) for a heterogeneous North Sea reservoir sandstone, indicating pore space (black), clay (dark gray), quartz (gray), feldspar (lighter gray) and carbonate cement (white). The side length of the images is 2.68 mm and the voxel resolution is 5.24 μm.

Permeability

The low Reynolds number flow of an incompressible Newtonian fluid is governed by the steady state Stokes equations

$$\mu\nabla^2\mathbf{v} = \nabla p\,, \tag{2}$$

$$\nabla\cdot\mathbf{v} = 0 \tag{3}$$

subject to the boundary condition **v** = 0 on the solid walls. **v** and p are the velocity and pressure, respectively. A D3Q19 Lattice Boltzmann algorithm (Jin *et al*., 2004) was used to solve the Stokes equations directly on the digitized images. The directional absolute permeabilities k_i are determined by applying a constant pressure gradient along the i-axes ($i = x, y, z$). The macroscopic flux is found by volumetric averaging of the local fluid velocity and k_i is determined from Darcy's law. We define the average permeability k to be the arithmetic average of the directional permeabilities.

Formation Factor

For the steady state conductivity problem, the governing local equations become the Laplace equation

$$\nabla \cdot \mathbf{J} = 0 \tag{4}$$

$$\mathbf{J} = \sigma_w \nabla \Phi \tag{5}$$

subject to the boundary condition $\nabla \Phi \cdot \mathbf{n} = 0$ on the solid walls. **J** is the electrical current, σ_w is the electrical conductivity of the fluid that fills the pore space, Φ is the potential or voltage, and **n** is the unit vector normal to the solid wall. Numerical solutions of the Laplace equation were obtained by a finite difference method (Øren and Bakke, 2002). A directional formation factor F_i is defined as the inverse of the effective electrical conductivity $F_i = \sigma_w/\sigma_i$. We define the average formation factor F to be the harmonic mean of the direction dependent formation factors.

Elastic Moduli

The local equations that govern the elastic behaviour of the heterogeneous media are the basic equations of elastostatics

$$\nabla \cdot \tau = 0 \tag{6}$$

$$\tau = \mathbf{C} : \varepsilon \quad \text{with} \quad \varepsilon = \frac{1}{2}\left[\nabla \mathbf{d} + (\nabla \mathbf{d})^T\right] \tag{7}$$

where τ and ε denote the stress and strain tensors, respectively, **d** is the displacement field, and **C** is the stiffness tensor. The above equations were solved via a finite element method using an energy representation of the linear elastic equations. Periodic boundary conditions are imposed on the faces of the digital images. The effective bulk and shear moduli are computed assuming isotropic linear elastic behaviour (Torquato, 2001).

Constitutive Relationships

Constitutive relationships, such as capillary pressure and relative permeability curves, are determined by simulating two-phase displacements (e.g., primary drainage, waterflood, secondary drainage) on the pore network representation of the computer generated rocks. The topology or connectivity of the pore network is determined by extracting the skeleton of the pore space. This is done by an ultimate dilation of the grains (Bakke and Øren, 1997). The vertices of the resulting Voronoi polyhedra define the pore bodies whilst the edges of the polyhedra identify the throats. With the mathematical skeleton as basis, we measure directly the size and volume of every pore body and throat using standard image analysis techniques (Øren and Bakke, 2003). Since the extracted pore network is in a one-to-one correspondence with the reconstructed pore space, we do not introduce any fitting or tuning parameters to match macroscopic parameters such as porosity and permeability.

In all the multiphase flow simulations it is assumed that capillary forces dominate at the pore scale. The basis for simulating capillary dominated displacements is the correct distribution of the fluids in the pore space. For two-phase flow, the equilibrium fluid distribution is governed by wettability and capillary pressure and can be found by applying the Young-Laplace equation for any imposed pressure difference between the phases. A clear and comprehensive discussion of all the mathematical details, including

the effects of wettability, involved in the simulations has been presented before (Øren *et al.*, 1998, Patzek, 2001, Øren and Bakke, 2003).
In the absence of viscous effects, fluid displacements proceed through a series of equilibrium fluid configurations. At each configuration we compute saturations, capillary pressure, and relative permeability. Macroscopic phase saturations are obtained by volume averaging the phase saturations in all pores and throats. The capillary pressure P_c is simply the entry capillary pressure associated with the last equilibrium configuration change. To compute relative permeabilities, the flow of each phase in the network must be specified. For laminar flow, the flow rate of fluid *i* between two connecting pores *I* and *J* is given by

$$q_{i,IJ} = \frac{g_{i,IJ}}{l_{IJ}}\left(P_{i,I} - P_{i,J}\right) \tag{8}$$

where l_{IJ} is the spacing between the pore centres. The effective conductance $g_{i,IJ}$ is assumed to be the harmonic mean of the conductances of the throat and the connected two half-pores. Expressions for the hydraulic conductance are derived from solutions of Stoke's equation in pores of different geometries and different fluid configurations (Øren *et al.*, 1998, Patzek and Kristensen, 2001). We invoke mass conservation at each pore

$$\sum_J q_{i,IJ} = \mathbf{0} \tag{9}$$

where *J* runs over all throats connected to pore *I*. Equations (8) and (9) give rise to a set of linear equations for the pore pressures that can be solved using standard techniques.

The absolute permeability *k* is computed initially when the network is fully saturated with water. From the computed pressure field one may calculate the total flow rate and thus the absolute permeability using Darcy's law. Relative permeabilities are computed similarly. The pressure in each phase is computed separately, assuming that all interfaces are fixed in place. The sum of flow rates through the inlet determines the macroscopic flow rate of the phase, which is inserted into Darcy's law to compute phase permeability k_i. Phase relative permeability is then given by $k_{ri} = k_i/k$. Constitutive relationships for a given displacement process are constructed by computing k_r and P_c for every 0.025 change in saturation.

RESULTS AND DISCUSSION

The two-point correlation functions, C_2, for the micro-CT and computer generated pore structures are in good agreement (see Figure 3). The presented functions are the average of the directional functions. The initial slope of C_2 allows an estimation of the specific surface areas (Yeong and Torquato, 1998) with 0.0205 μm^{-1} and 0.0192 μm^{-1} for the MCT and PBM samples, respectively. The decay length, determined at $C_2 = 0$, is found with $L = 0.72$ mm in both samples. The tail in C_2 indicates a longer range structure in the samples. This is attributed to the wide grain size distribution and the occurrence of clays and carbonate cementation.

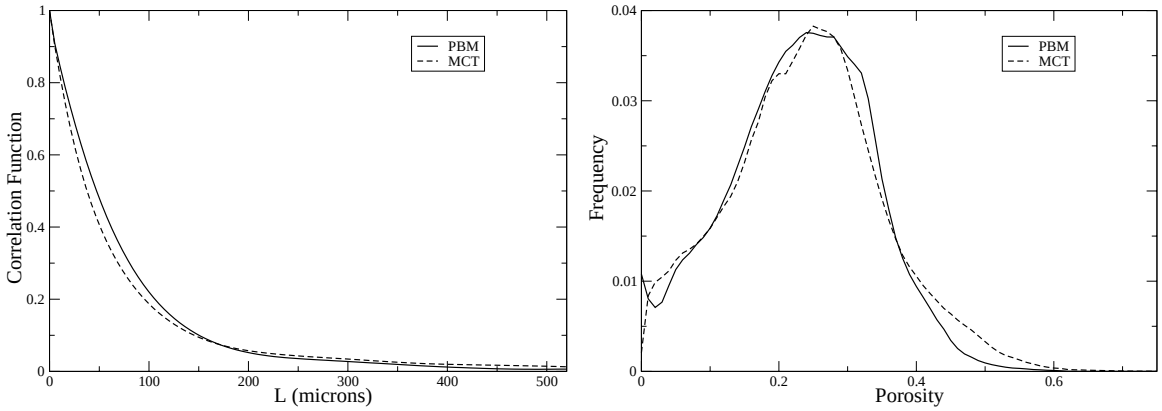

Figure 3. Average two-point correlation functions (left) and 3D local porosity distributions $\mu(\phi,L$=0.39mm) (right) for the MCT and PBM samples.

Table 1. Computed transport properties of the micro-CT and reconstructed samples.

Sample	**Porosity**	F_x	F_y	F_z	F	k_x**(mD)**	k_y**(mD)**	k_z**(mD)**	k**(mD)**
MCT	0.240	12.7	16.6	12.2	13.6	5853	4322	6334	5502
PBM	0.243	10.8	10.9	11.0	10.9	6515	6132	6015	6221

The 3D local porosity distributions, $\mu(\phi,L)$, (Hilfer, 1991) for the two samples are shown in Figure 3 (right). $\mu(\phi,L)$ measures the empirical probability of finding the local porosity ϕ in a cubic cell of linear dimension L. The porosity distributions displayed in Figure 3 were computed with L = 0.39 mm. Both the width (variance in porosity) and the peak (most probable porosity) of the distributions are similar. The higher value at the origin for the reconstructed sample indicates that larger regions of matrix occur more frequently. This is consistent with the calculations of the characteristic length L^* (Biswal *et al.*, 1999). The calculations yielded L^* = 0.84 mm and L^* = 0.79 mm for the PBM and MCT samples, respectively. L^* gives the side length of the largest cube that can be fit into the matrix space and can be viewed as a measure of the size of the largest grain.

The computed directional and averaged formation factors and absolute permeabilities for the entire sample sizes (i.e., 512^3 voxels with resolution of 5.24 μm) are compiled in Table 1. The PBM sample is fairly isotropic in its transport properties whilst the MCT sample is slightly an-isotropic with a higher formation factor and a lower permeability in the *y*-direction. Compared to the MCT sample, the reconstructed pore structure over-predicts the average absolute permeability with 13% (5503 mD vs. 6221 mD) and under-predicts the average formation factor with 20% (13.6 vs. 10.9). Since the porosity of the two samples is similar, this implies that the tortuousity of the MCT sample is larger than that of the PBM sample. The experimentally determined absolute permeability measured on the larger core plug was 4370 mD. The permeability and formation factor computed on the pore network representation of the reconstructed sample was 6347 mD and 16.5, respectively.

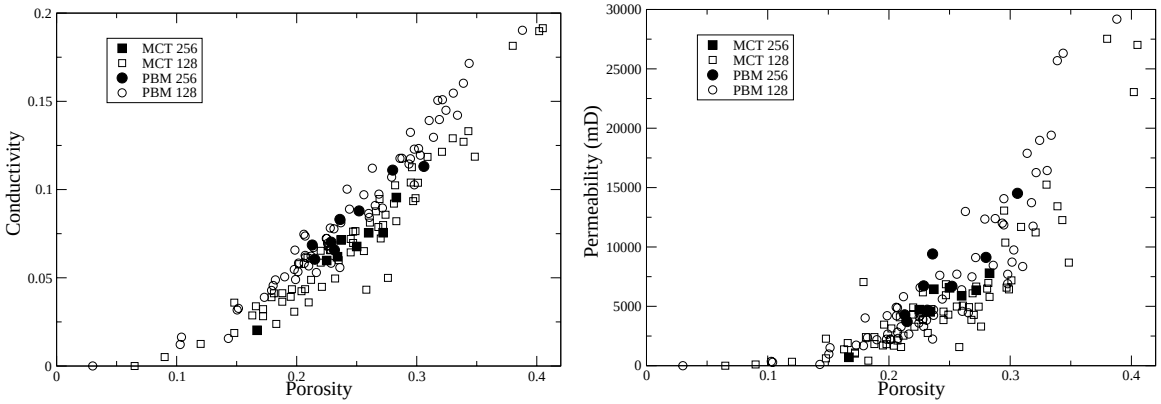

Figure 4. Computed electrical conductivity (left) and absolute permeability (right) versus porosity trends for the MCT and PBM samples. Shown are calculations on sub-samples of size 128^3 and 256^3 voxels.

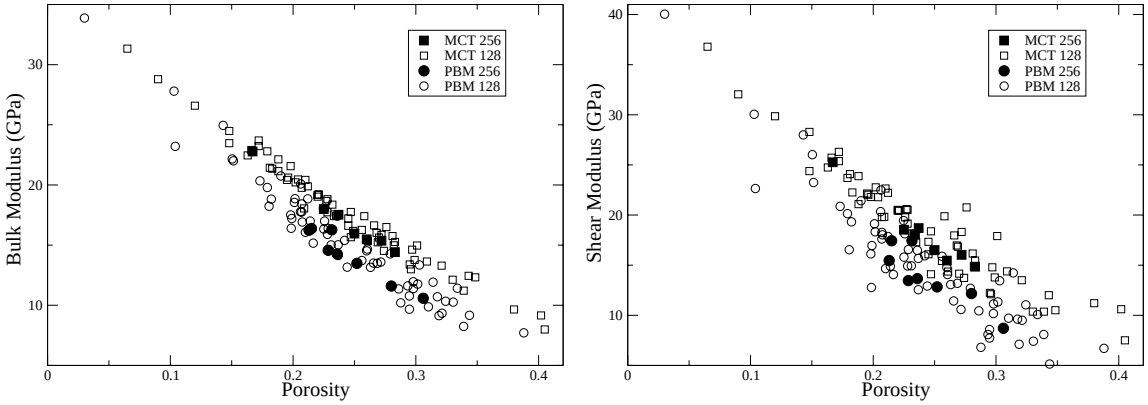

Figure 5. Computed bulk modulus (left) and shear modulus (right) versus porosity trends for the MCT and PBM samples. Shown are calculations on sub-samples of size 128^3 and 256^3 voxels.

Transport properties computed on non-overlapping sub-samples are displayed in Figure 4. The side lengths of the cubic sub-samples are 0.67 mm (128^3 voxels) and 1.34 mm (256^3 voxels) and thus in the range of the determined correlation lengths of the samples (L = 0.72 mm for C_2 = 0). The trend in absolute permeability versus porosity is similar for both the micro-CT and the computer generated pore structure. The computed electrical conductivity versus porosity trend shows that the reconstructed pore structure supports slightly higher conductances, or predicts lower formation factors, than the microtomographic image. A possible explanation might be found in the explicit accounting of small pores in the PBM sample. These pores contribute significantly to the electrical conductance but have little effect on the absolute permeability.

The calculation of the bulk and shear moduli are presented in Figure 5. Results are shown again for sub-samples of size 128^3 and 256^3 voxels and indicate the variability contained in each sample. The trends plotted against porosity are near linear, with a larger scatter at high porosities. A difference in slope is apparent between the MCT and PBM data.

This yields a small, but systematic under-prediction of the elastic moduli for the reconstructed pore structure, or vice versa an over-prediction in the tomographic image. The elastic moduli depend strongly on the representation of the grain to grain contacts. Whether the influence of image processing (i.e., thresholding) in the MCT sample accounts for this effect is not determined, yet we have indications supporting such interpretation.

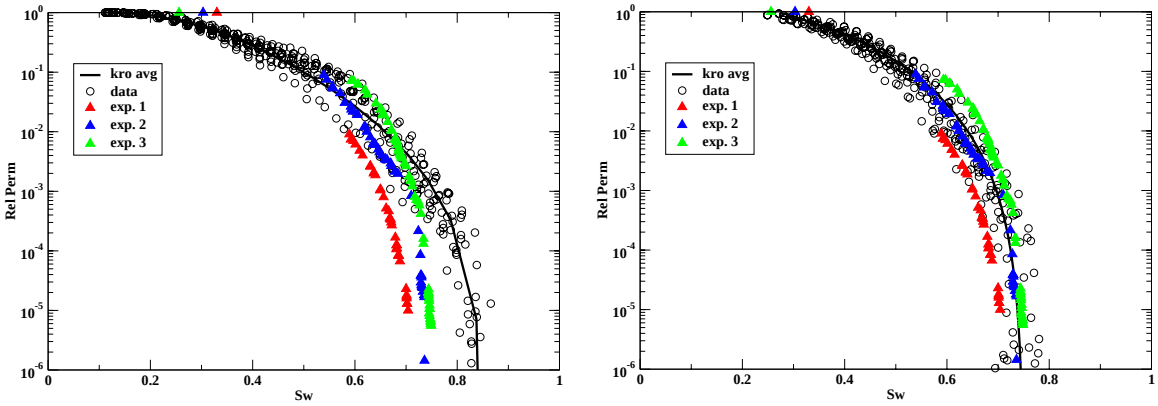

Figure 6. Comparison between simulated and centrifuge measured oil relative permeabilities. The initial water saturation for the simulated results is $S_{wi} \sqcup 0.15$ (left) and $S_{wi} \sqcup 0.29$ (right).

Waterflood oil and water relative permeabilities were computed on all 10 realizations of the reconstructed sample. This was done by first simulating primary drainage at strongly water wet conditions to establish initial water saturation S_{wi}. Next, a waterflood was simulated at the recommended wettability state ($I_{wo} \sqcup 0.5$). The target I_{wo} was achieved by letting 40% of the oil invaded pores become oil wet. The advancing contact angle, θ_a, for the oil wet pores and throats was randomly distributed between $110^o < \theta_a < 160^o$ whilst for the water wet pores and throats, θ_a was randomly distributed in the range $20^o < \theta_a < 60^o$. The computed I_{wo} for the different realizations varied between 0.4 and 0.6. In Figure 6 (left), the computed oil relative permeabilities are compared with centrifuge measured oil relative permeabilities. The experimental data stems from three different core plugs. The computed results tend to over-predict the measured oil relative permeabilities, especially at low oil saturations, and the simulated residual oil saturation, S_{orw}, is smaller than that determined experimentally (0.15 versus 0.25).

The S_{wi} values for the experimental core plugs ranged between 0.26 and 0.33. This is significantly higher than the simulated value of $S_{wi} \sqcup 0.15$. It is also higher than that observed in the field. The reason for this discrepancy is most likely experimental difficulties caused by the fact the core samples are poorly consolidated and thus easily damaged at the high rotational speeds necessary to reach low initial water saturations. However, it is well known that the initial water saturation can have a significant effect on the subsequent waterflood, especially for non water wet samples (Jadhunandan and Morrow, 1995). To allow a direct comparison with the experimental data, we redid all the

simulations with S_{wi} values similar to the experimental ones. This was done by terminating the primary drainage simulations at $S_{wi} \approx 0.29$. The pore-level distribution of wettability (i.e., contact angles and fraction oil wet pores) was the same as before.

The results are shown in Figure 6 (right). The agreement between measured and computed oil relative permeabilities has improved notably. While the pore-level distribution of wettability was the same as before, the computed S_{orw} has increased and is similar to the measured values. The increase in S_{orw} is primarily caused by reduced oil film stability in mixed wet pores. The negative capillary pressure at which oil films that exists in corners and crevices of the pore space collapses is directly proportional to the maximum capillary pressure, and thus S_{wi}, reached during primary drainage (Blunt, 1997, Øren *et al*., 1998). At higher S_{wi} (i.e., smaller maximum capillary pressure), the oil films will be thinner and less conductive. This, in turn, reduces the oil relative permeability at low oil saturations where much of the oil is forced to flow through films.

Figure 7 compares simulated water and oil relative permeabilities with measured steady state relative permeabilities. The steady state experiments were done on two composite cores, each made up of four core plugs butted together. Even though the simulated results tend to slightly over-estimate the water relative permeability, Figure 7 shows that almost all of the measured data fall within the scatter of the simulated data. This agreement between measured and predicted relative permeabilities is rather encouraging, especially considering the complex nature of the sandstone lithofacies and the uncertainty in wettability. Although we need to examine a larger group of heterogeneous rock samples, these results suggest that computer generated rocks combined with numerical calculations might be a viable approach to *a priori* derive important reservoir rock properties.

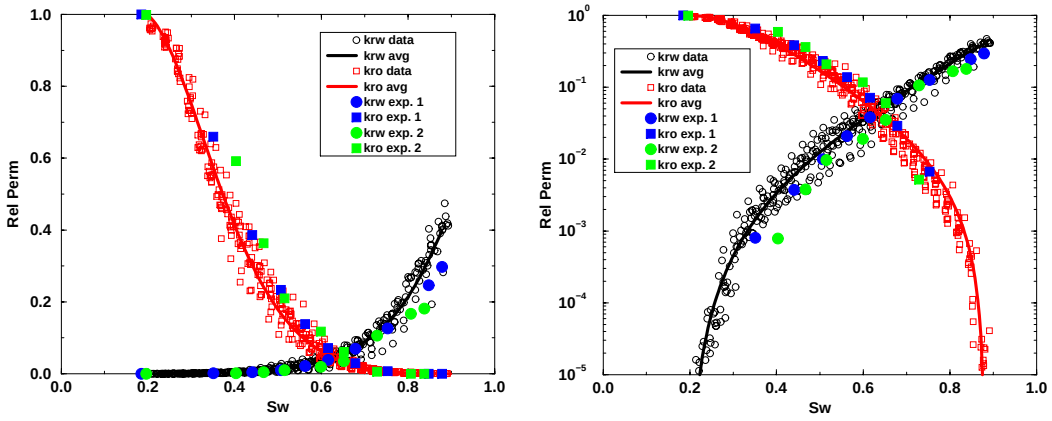

Figure 7. Comparison between predicted and steady state determined waterflood relative permeabilities. The initial water saturation for the experiments and for the simulations is similar with $S_{wi} \approx 0.19$.

CONCLUSIONS

We investigated the predictive capabilities of direct pore scale simulations of material and transport related effective properties for a heterogeneous channel sandstone in a North Sea reservoir. The study reveals an excellent agreement of the effective properties for micro-CT images and geologically based reconstructed samples. Computed waterflood relative permeabilities for the computer generated rocks are in good agreement with measured data. Our simulations show that for mixed wet samples, the oil relative permeability and the residual oil saturation critically depend on the initial water saturation at the start of the displacement. This is due to the fact that the stability of oil films present in mixed wet pores depends directly on the maximum capillary pressure, and thus the $S_{wi,}$ reached during primary drainage.

Our results demonstrate the potential and feasibility of combining computer generated rocks with numerical calculations to derive rock and flow properties for reservoir rocks and to augment the analysis and interpretation of experimentally derived SCAL data. This can lead to the development of type curves for properties and cross-property relations, which are more readily constructed numerically than by experimentation. This presents exciting possibilities of bridging the technology gap that exists today between detailed geological models and the lack thereof for the associated reservoir rock properties.

REFERENCES

1. Adler, P.M., Jacquin, C.G., and Quiblier, J.A., “Flow in simulated porous media”, *Int. J. Multiphase Flow*, (1990), **16**, 691-712.
2. Arns, C.H., Knackstedt, M.A., Pinczewski, V., and Garboczi, E.J., “Computation of linear elastic properties from microtomographic images: Methodlogy and agreement between theory and experiments”, *Geophysics*, (2002), **67**, 1396-1405.
3. Arns, C.H., Knackstedt, M.A., Pinczewski, V., and Martys, N.S., “Virtual permeametry on microtomographic images”, *J. Petroleum Science and Engineering*, (2004), **45**, 41-46.
4. Bakke, S., and Øren, P.E., “3-D Pore-Scale Modeling of Sandstones and flow Simulations in the Pore Networks”, *SPE Journal*, (1997), **2**, 136-149.
5. Biswal, B., Manswart, C., Hilfer, R., Bakke, S., and Øren, P.E., “Quantitative analysis of experimental and synthetic microstructures of sedimentary rocks”, *Physica A*, (1999), **273**, 452-475.
6. Blunt, M., “Pore level modeling of the effects of wettability”, *SPE Journal*, (1997), **2**, 494-510.
7. Bryant, S.L., Cade, C.A., and Melor, D.W., ”Permeability prediction from geological models”, *AAPG Bulletin*, (1993), **77**, 1338-1350.
8. Hazlett, R.D., “Statistical characterization and stochastic modeling of pore networks in relation to fluid flow”, *Math. Geol*., (1997), **29**, 801-822.
9. Hilfer, R., “Geometric and dielectric characterization of porous media”, *Physical Review B*, (1991), 60-75.

10. Jadhunandan, P.P. and Morrow, N.R., "Effect of wettability on waterflood recovery for crude-oil/brine/rock systems", *SPE Reservoir Engineering*, (1995), **10**, 40-46.
11. Jin, G., Patzek, T.W., and Silin, D.B., "Direct Prediction of the Absolute Permeability of Unconsolidated and Consolidated Reservoir Rock", *SPE paper* 90084, (2004), presented at the SPE ATCE, Houston, TX, September 2004.
12. Jin, G., Patzek, T.W., and Silin, D.B "Physics based Reconstruction of Sedimentary Rocks", *SPE paper* 85387, (2003), Long Beach CA., 19-24 May, 2003.
13. Knackstedt, M.A., Arns, C.H., Limaye, A., Sakellariou, A, Senden, t.J., Sheppard, A.P., Sok, R.M., and Pinczewski, W.V., "Digital Core Laboratory: Properties of reservoir core derived from 3D images', *SPE paper* 87009, (2204), Kuala Lumpur, Malyasia, 2004.
14. Lerdahl, T.R., Øren,P.E., and Bakke, S., "A predictive network model for three-phase flow in porous media", *SPE paper* 59311, (2000), SPE/DOE Symposium on EOR, Tulsa, OK, April 3-5, 2000.
15. Manswart, C., Aaltosalmi, U., Koponen, A., Hilfer, R., and Timonen, J., "Lattice-Boltzmann and finite difference simulations for the permeability for three-dimensional porous media", *Physical Review E*, (2002), **66**, 016702.
16. Patzek, T.W., "Verification of a complete network simulator for drainage and imbibition", *SPE Journal*, (2001), **6**, 144-156.
17. Patzek, T.W., and Kristensen, J.D., "Shape factor and hydraulic conductance in non-circular capillaries: II. Two-phase creeping flow", *J. Colloid & Interface Sci*., (2001), **236**, 305-317.
18. Piri, M., and Blunt, M., "Three-dimensional mixed-wet random pore-scale network model of two- and three-phase flow in porous media", *Physical Review E*, (2005), **71**, 026301.
19. Torquato, S., *Random Heterogenous Material – Microstructures and Macroscopic Propereties*, Springer Verlag (2001), New York, 324-332.
20. Valvatne, P.H., and Blunt, M., "Predictive pore-scale modeling of two-phase flow in mixed wet media", *Water Resources Research*, (2004), **40**, 1-21.
21. Yeoung, C.L.Y., and Torquato, S., "Reconstructing random media", *Phys. Rev. E*, (1998), **57**, 495-506.
22. Øren, P.E., Bakke, S., and Arntzen, O.J., "Extending Predictive Capabilities to Network Models", *SPE Journal*, (1998), **3**, 324-336.
23. Øren, P.E., and Bakke, S., "Process Based Reconstruction of Sandstones and Prediction of Transport Properties", *Transport in Porous Media*, (2002), **46**, 311-314.
24. Øren, P.E., Antonsen, F, Rueslåtten, H., and Bakke, S., "Numerical Simulation of NMR Responses for Improved Interpretations of NMR Measurements in Reservoir Rocks", *SPE paper* 77398, (2002), presented at the SPE ATCE, San Antonio, TX, Sept.29 – Oct.2, 2002.
25. Øren, P.E., and Bakke, S., "Reconstruction of Berea sandstone and pore-scale modeling of wettability effects", *J. Petroleum Science and Engineering*, (2003), **39**, 177-199.